Needle-Like Multifunctional Biphasic Microfiber for Minimally Invasive Implantable Bioelectronics

Seonghyeon Nam, Gi Doo Cha, Sung-Hyuk Sunwoo, Jae Hwan Jeong, Hyejeong Kang, Ok Kyu Park, Kyeong-Yeon Lee, Seil Oh, Taeghwan Hyeon, Seung Hong Choi,* Seung-Pyo Lee,* and Dae-Hyeong Kim*

Implantable bioelectronics has attracted significant attention in electroceuticals and clinical medicine for precise diagnosis and efficient treatment of target diseases. However, conventional rigid implantable devices face challenges such as poor tissue-device interface and unavoidable tissue damage during surgical implantation. Despite continuous efforts to utilize various soft materials to address such issues, their practical applications remain limited. Here, a needle-like stretchable microfiber composed of a phase-convertible liquid metal (LM) core and a multifunctional nanocomposite shell for minimally invasive soft bioelectronics is reported. The sharp tapered microfiber can be stiffened by freezing akin to a conventional needle to penetrate soft tissue with minimal incision. Once implanted in vivo where the LM melts, unlike conventional stiff needles, it regains soft mechanical properties, which facilitate a seamless tissue-device interface. The nanocomposite incorporating with functional nanomaterials exhibits both low impedance and the ability to detect physiological pH, providing biosensing and stimulation capabilities. The fluidic LM embedded in the nanocomposite shell enables high stretchability and strain-insensitive electrical properties. This multifunctional biphasic microfiber conforms to the surfaces of the stomach, muscle, and heart, offering a promising approach for electrophysiological recording, pH sensing, electrical stimulation, and radiofrequency ablation in vivo.

1. Introduction

Advances in implantable medical devices, such as cardiac pacemakers, ablation catheters, and electrophysiological sensors, have significantly contributed to personalized healthcare and clinical medicine.[1–3] Electroceutical applications of these implantable devices hold promise in the drug-free treatment of various diseases through vagus nerve and other nervous system stimulations.[4–6] However, the rigid devices face challenges due to poor tissue-device contact and unwanted mechanical damage to the interfacing organs. These issues can reduce the signal-to-noise ratio in biosensing, lead to electrical stimulation fatigue, and cause scar formation and inflammatory responses.[7–9] To address these challenges, soft bio-integrated electronics has been proposed.[10–14] In particular, intrinsically soft bioelectronics, composed entirely of stretchable materials, show promise for next-generation biomedical devices that are mechanically compatible with the soft human body.[15–17]

S. Nam, H. Kang, O. K. Park, T. Hyeon, S. H. Choi, S.-P. Lee, D.-H. Kim
Center for Nanoparticle Research
Institute for Basic Science (IBS)
Seoul 08826, Republic of Korea
E-mail: verocay1@snu.ac.kr; sproll1@snu.ac.kr; dkim98@snu.ac.kr

S. Nam, T. Hyeon, D.-H. Kim
School of Chemical and Biological Engineering, Institute of Chemical Processes
Seoul National University
Seoul 08826, Republic of Korea

G. D. Cha
Department of Systems Biotechnology
Chung-Ang University
Ansung 17546, Republic of Korea

S.-H. Sunwoo
Department of Chemical Engineering
Kumoh National Institute of Technology
Gumi 39177, Republic of Korea

J. H. Jeong
Department of Chemical Engineering
Stanford University
Stanford, CA 94305, USA

O. K. Park, S. H. Choi
Department of Radiology
Seoul National University College of Medicine
Seoul 03080, Republic of Korea

K.-Y. Lee, S. Oh, S.-P. Lee
Division of Cardiology, Department of Internal Medicine
Seoul National University Hospital
Seoul 03080, Republic of Korea

S. Oh, S.-P. Lee
Department of Internal Medicine
Seoul National University College of Medicine
Seoul 03080, Republic of Korea

Among various material candidates for fabricating intrinsically soft bioelectronics, elastomeric nanocomposites[18–21] and liquid metal (LM) alloys[22–24] have garnered considerable attention. Elastomeric nanocomposites offer high conductivity, low impedance, and high stretchability. They can also be additionally functionalized with nanoparticles for diverse biomedical applications.[25–27] On the other hand, LMs exhibit exceptional conductivity, strain-insensitive electrical properties, and solid-liquid phase-changing properties.[28–32] Despite these unique features and advantages, their medical device applications have been limited. The performance of the nanocomposites tends to deteriorate under mechanical deformations, and hysteresis in their electrical properties is often observed. LMs require elaborately designed encapsulation layers to ensure long-term, reliable operation within the body.[33,34] Additionally, the high surface tension and native oxide layer of LMs present additional challenges that hinder their medical device applications.[35,36]

Another crucial aspect necessary for the practical application of soft bioelectronics, yet often challenging to achieve, is the minimally invasive deployment of the soft bioelectronic device to the targeted location within the body. The potential for minimally invasive deployment can streamline surgical procedures, offering faster and safer interventions that reduce patient discomfort and enhance the feasibility of soft bioelectronics for implantable electroceuticals.[37–39] However, the inherently flexible and deformable mechanical properties of intrinsically soft and stretchable bioelectronics make their handling and minimally invasive deployment significantly challenging. Recent studies on robot-assisted surgery show promise in addressing these challenges, but further developments are needed to improve the dexterity in handling mechanically fragile soft devices, adapt to dynamic body environments, and reduce operating costs. Therefore, there is a pressing need to develop a simple yet effective method for the minimally invasive deployment method of soft bioelectronics to target internal organs.

In this study, we present a needle-like stretchable microfiber comprising a phase-convertible LM core and a multifunctional nanocomposite shell, designed specifically for minimally invasive soft bioelectronics. The microfiber can be deployed inside the body through stiffness control by leveraging the phase-convertible behavior of LM. It is solidified using freeze-spraying, providing the temporary rigidity to penetrate soft tissues akin to a conventional needle. Subsequently, it liquefies at body temperature, recovering its original softness. The stretchable nanocomposite shell, with the aid of functional filler nanoparticles, forms a reliable interface between the fluidic LM and biological tissues, demonstrating low impedance and pH sensing capabilities. Through biosensing and stimulation experiments, we showcase its gastric, muscular, and cardiac electroceutical applications in vivo, highlighting the translational potential of the microfiber for various theragnostic cases.

2. Results and Discussion

2.1. Material Design of the Needle-Like Injectable Microfiber

The needle-like stretchable conductive multifunctional microfiber can be deployed to a target internal organ or tissue in a minimally invasive manner. This biphasic microfiber consists of a phase-convertible LM inner core and a multifunctional nanocomposite outer shell (**Figure 1a-i**), combining the advantageous properties of both materials such as intrinsic softness, high stretchability, high conductivity, and strain-insensitivity (Figure S1 and Table S1, Supporting Information). In addition, the integration of auxiliary micro/nanoparticles on the nanocomposite surface provides additional functions such as pH sensitivity and low impedance to the microfiber. These features allow the microfiber to serve reliable electroceutical applications (i.e., sensing (Figure 1a-ii) and stimulation (Figure 1a-iii) as an implantable bioelectronics for electrophysiological recording, pH sensing, electrical stimulation, and radiofrequency ablation, on dynamically moving organs[40] (Figure S2, Supporting Information).

The minimally invasive implantation of the microfiber (Figure 1a-iv) harnesses not only the phase-transition characteristics of LMs (eutectic gallium-indium; whose melting temperature is ≈15.5 °C),[41] but also the geometric engineering of the microfiber.[42,43] The microfiber is thin and long (≈20 cm) enough to reach internal organs while maintaining a wired connection with external equipment (Figure 1b). Before implantation, the intrinsically soft microfiber stiffens like a needle frozen by freeze-spraying. The frozen microfiber, with a tapered tip as sharp as a commercial 24G stainless needle tip (diameter < 300 μm) (Figure 1b-i), is rigid enough to penetrate tissues. Once injected, the microfiber restores its original softness inside the body due to the solid-to-liquid phase transition of the LM, whose mechanical softness becomes comparable to that of the target tissue. The arrowhead-shaped anchor in the middle of the microfiber (Figure 1b-ii) ensures its stable fixation in the internal cavity during operation. Successful minimally invasive administration of the microfiber into the rat heart was demonstrated in vivo, as confirmed by visual (Figure 1c) and ultrasound imaging (Figures 1d and S3, Supporting Information) observations.

The LM core of the microfiber is encapsulated by an elastomeric nanocomposite shell, composed of a mixture of gold-coated silver nanowires (Ag-Au NWs), platinum black (Pt black) microparticles and/or IrO_2 nanoparticles, along with an elastic block copolymer (poly(styrene-butadiene-styrene); SBS) (Figure 1b-iii). The Ag-Au NWs, characterized by their high aspect ratio (length:diameter = 250:1), form a dense percolation network that enables high conductivity.[44–46] Functional additive particles (e.g., Pt black microparticles and IrO_2 nanoparticles) are integrated within the nanocomposite to provide low impedance and pH sensing capabilities, respectively.[47] The fabrication process (Figure S4, Supporting Information) used to create the LM core and nanocomposite shell structure is detailed in the Experimental Section. This core–shell structure was verified through cross-sectional scanning electron microscopy observation combined with energy dispersive X-ray spectroscopy analysis (SEM-EDS; Figure 1b-iv).

2.2. Temporary Stiffness Control of the Microfiber by Phase Transition of Liquid Metal for Minimally Invasive Administration

The solidification of LM through freeze-spraying imparts high stiffness to the microfiber (**Figure 2a**), allowing it to penetrate tissues independently without the need for invasive surgical tools.
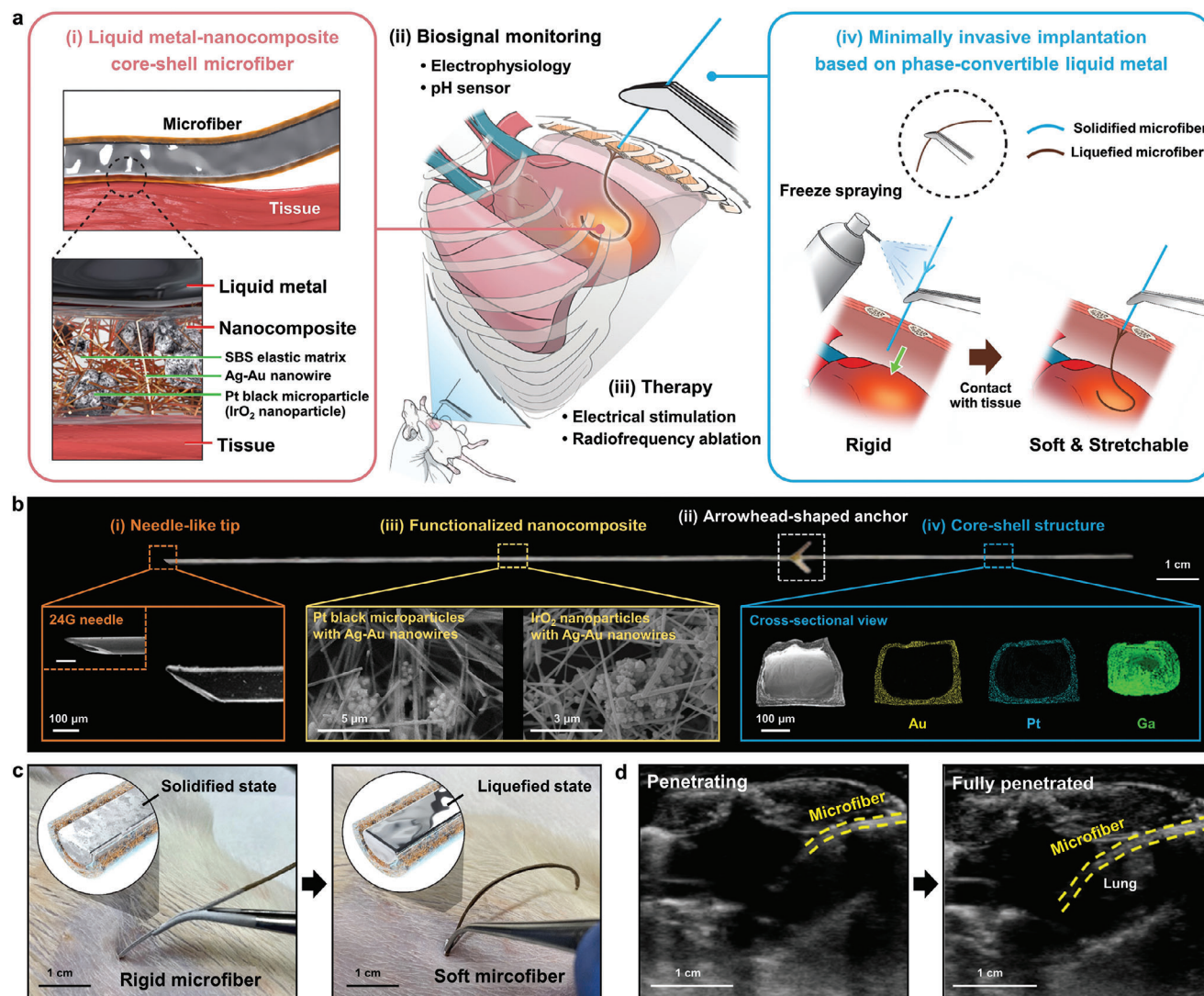
ADVANCED
SCIENCE NEWS

www.advancedsciencenews.com

ADVANCED
MATERIALS

www.advmat.de

Figure 1. Material design and implantation of a needle-like injectable microfiber. a) Schematic illustration of the microfiber structure and its minimally invasive administration protocol. i) The microfiber composed of liquid metal core and nanocomposite (Ag-Au nanowire, Pt black microparticle and/or IrO₂ nanoparticle, and elastic matrix) shell is conformally applied to the tissue surface and performs ii) biosignal monitoring and iii) electroceutical therapies. iv) The soft microfiber is frozen to be rigid, like a needle, by freeze-spraying. The solidified microfiber can penetrate tissues, and it recovers its original softness in response to the body temperature after implantation. b) Optical image of the microfiber. i) Scanning electron microscopic image of the microfiber's tapered tip compared to a commercial 24G needle tip (inset). ii) The arrowhead-shaped anchor enables its stable fixation in the internal cavity. iii) The nanocomposite shell consists of Ag-Au nanowire and functional micro/nanoparticles and encompasses the liquid metal core (eutectic gallium-indium), which was confirmed by iv) cross-sectional scanning electron microscopic images with energy-dispersive spectroscopy. c) Optical images of the solidified microfiber penetrating the rat tissue through the skin of the intercostal region (left) and the liquefied microfiber that softened to be conformally applied to the organ surfaces (right). d) Sonographic images of the solidified microfiber penetrating the rat tissue (left) and the liquefied microfiber that softened to be conformally applied to the myocardial surface (right).

Following implantation, the microfiber interfaces with the target internal organ at body temperature, causing the frozen LM to liquefy and the microfiber to regain its original tissue-like softness (Figure 2b). Concurrently, the arrowhead-shaped anchor in the middle of the microfiber fixes the microfiber at the internal cavity to maintain stable tissue interfacing (Figure S5a, Supporting Information). This temporary stiffness modulation relies on the phase transition of LM near room temperature (15.5 °C), easily induced by freeze-spraying (<0 °C), as confirmed by cryo-scanning electron microscopy (Figure S5b,c, Supporting Infor-

mation). To assess the penetration capability of the microfiber, we conducted insertion experiments using 2 wt% agar hydrogel as an artificial tissue.[48] The solidified microfiber successfully penetrated the artificial tissue (Figure 2c), whereas the liquefied microfiber did not (Figure 2d). This difference is evident in Video S1 and Figure S5d,e, Supporting Information.

Numerical simulation was employed to analyze temperature-dependent stiffness control. The Von Mises stresses of the microfiber in solidified and liquefied states are compared with the tissue modulus. The elastic modulus of the solidified microfiber
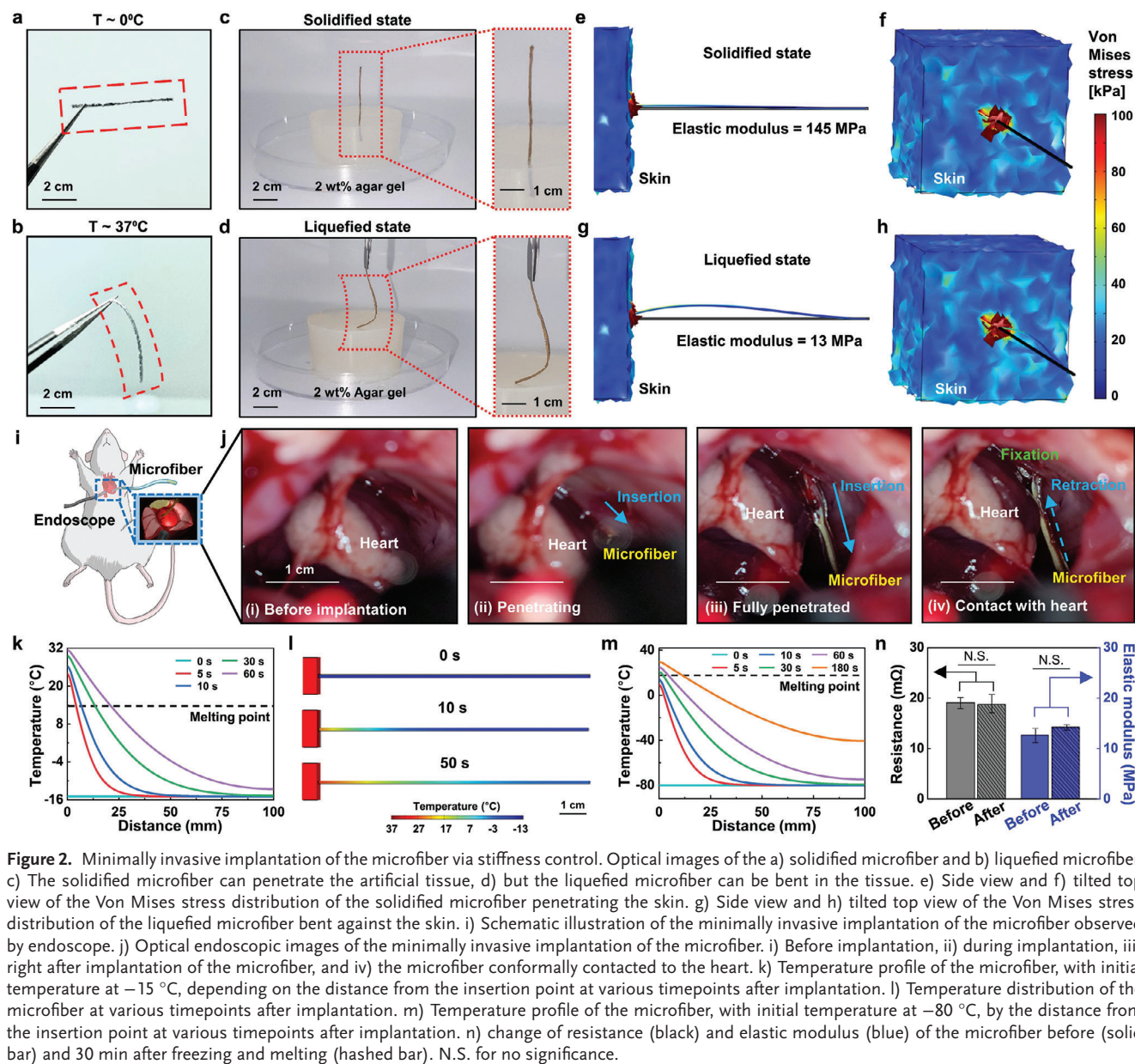
2404101 (3 of 12)

Figure 2. Minimally invasive implantation of the microfiber via stiffness control. Optical images of the a) solidified microfiber and b) liquefied microfiber. c) The solidified microfiber can penetrate the artificial tissue, d) but the liquefied microfiber can be bent in the tissue. e) Side view and f) tilted top view of the Von Mises stress distribution of the solidified microfiber penetrating the skin. g) Side view and h) tilted top view of the Von Mises stress distribution of the liquefied microfiber bent against the skin. i) Schematic illustration of the minimally invasive implantation of the microfiber observed by endoscope. j) Optical endoscopic images of the minimally invasive implantation of the microfiber. i) Before implantation, ii) during implantation, iii) right after implantation of the microfiber, and iv) the microfiber conformally contacted to the heart. k) Temperature profile of the microfiber, with initial temperature at −15 °C, depending on the distance from the insertion point at various timepoints after implantation. l) Temperature distribution of the microfiber at various timepoints after implantation. m) Temperature profile of the microfiber, with initial temperature at −80 °C, by the distance from the insertion point at various timepoints after implantation. n) change of resistance (black) and elastic modulus (blue) of the microfiber before (solid bar) and 30 min after freezing and melting (hashed bar). N.S. for no significance.

(145 MPa) is sufficiently high to penetrate the tissue (Figure 2e,f), while the softness of the liquefied microfiber matched that of the tissue (Figure 2g,h). In vivo injection of the needle-like microfiber was also demonstrated by visualization using an endoscope (Figure 2i). The solidified microfiber was implanted into the rat's thoracic cavity, penetrating the rib cage muscles and connective tissues. Upon exposure to body temperature, the microfiber softened, establishing conformal contact with the beating heart without harming nearby organs like the lungs and avoiding damage to the contacted myocardium itself. The arrowhead-shaped anchor prevents the microfiber retraction and verifies its position upon implantation (Figure 2j).

Temperature plays a crucial role in determining the stiffness of the microfiber, with the time to reach thermal equilibrium estimated through simulation. After implantation, the temperature of the microfiber (- 15 °C) in a solidified state begins to rise (Figure 2k,l) when exposed to body temperature (≈37 °C). However, only a minor part of the microfiber (e.g., within 10 mm from the insertion point) exceeds the melting temperature of LM (15.5 °C; Figure 2k black line) at 10 s post-implantation. After 1 min, the temperature of the microfiber beyond 25 mm from the insertion point remains below the melting temperature of LM, minimizing tissue damage at the insertion site, while maintaining high enough rigidity at the shaft of the microfiber. The retention time of temporary rigidity can be controlled by manipulating the initial temperature (Figure 2m). We confirmed that this strategy, involving phase transition of the LM, accompanies minimal changes in the electrical and mechanical performance of the microfiber – changes in the resistance and modulus (Figure 2n) between freezing and melting are negligible.
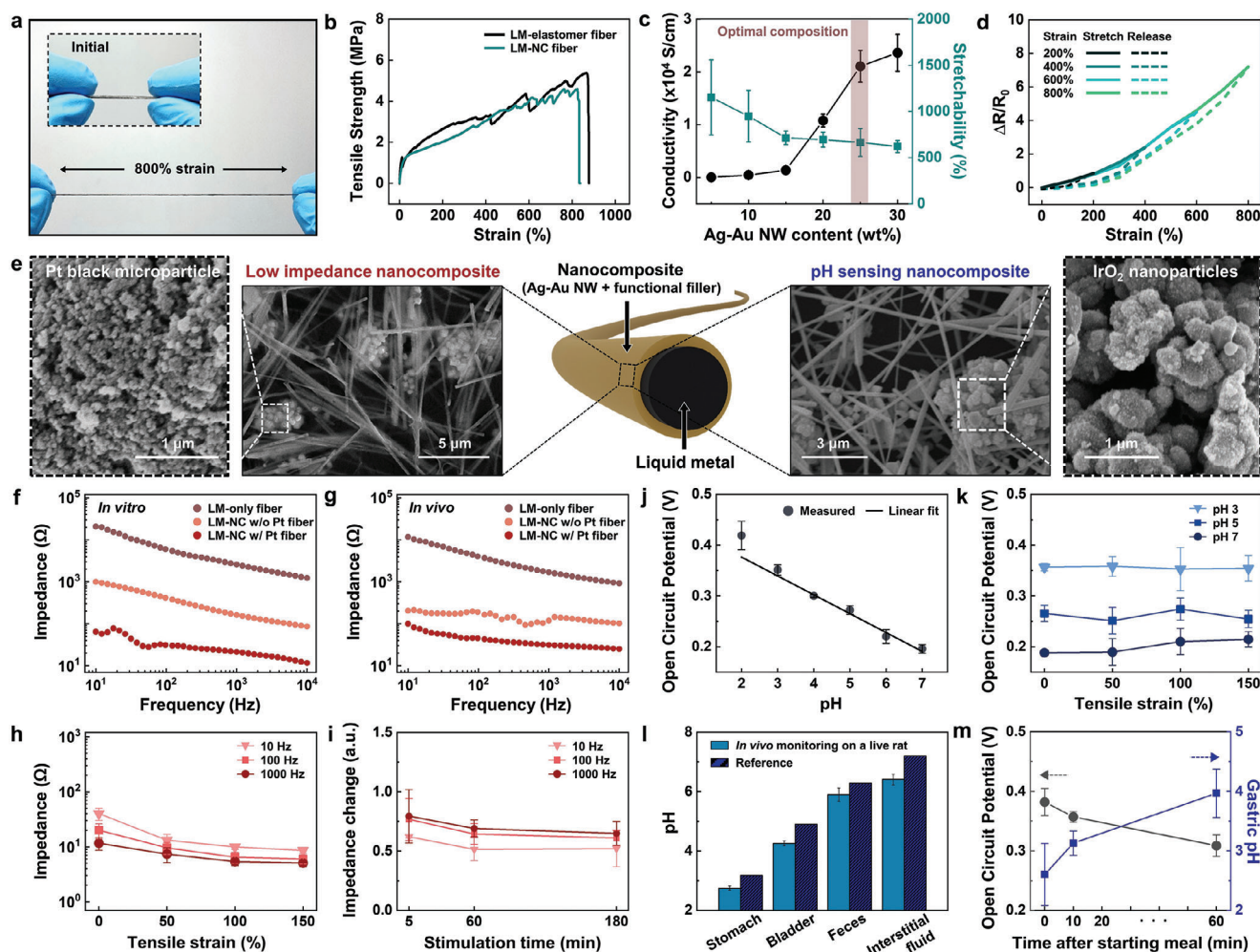
**ADVANCED
SCIENCE NEWS**

www.advancedsciencenews.com

**ADVANCED
MATERIALS**

www.advmat.de

Figure 3. Mechanical, electrical, and electrochemical characterization of the microfiber. a) Optical image of the microfiber before (inset) and after stretching. b) Stress–strain curve of the microfiber compared to LM-elastomer (SBS) microfiber without nanofillers. c) Conductivity (left axis) and stretchability (right axis) change of the microfiber at different contents of Ag-Au nanowires (5 to 30 wt%). d) Relative resistance change of the microfiber under tensile strain. e) Scanning electron microscopic images of the microfiber surface with Pt black microparticles (left) and IrO$_2$ nanoparticles (right). Electrochemical impedance spectroscopy (EIS) curves for an LM-only microfiber, an LM-NC microfiber without Pt black microparticles, and an LM-NC microfiber with Pt black microparticles f) in vitro, and g) in vivo. Impedance change of the microfiber for 10–1000 Hz h) under tensile strain and i) after applying electrical stimulation through the microfiber. j) Open circuit potential of the microfiber in buffer solution with different pH values. The black line is a linear fit to the measured data (gray spheres). k) Change in open circuit potential of the microfiber under tensile strain. l) pH measurements in various rat organs. m) Change in open circuit potential (black) and pH (blue) measured from the rat stomach depending on the time after food intake.

2.3. Mechanical, Electrical, and Electrochemical Performance of the Microfiber

The core–shell structure, that is, LM core and nanocomposite shell, allows for the microfiber to display advantageous properties of both LM and the nanocomposite: high conductivity, high stretchability, strain-insensitivity, reliable tissue-device interfacing, and multi-functionalization capability (e.g., low impedance and pH sensitivity). Consequently, the microfiber demonstrates excellent mechanical, electrical, and electrochemical performance, simultaneously.

The stretchable nature of the microfiber is well-suited for bioelectronics applications in dynamic organs. For example, the microfiber can stretch up to 800% without fracturing (**Figure** 3a), which is sufficient to accommodate structural changes in dy-

namic internal organs (e.g., heart: 20%, stomach: 30%, bladder: 80%).[49] The stable encapsulation of LM and filler incorporation by the nanocomposite, even under repetitive mechanical deformations (Figure S6, Supporting Information), as confirmed by Inductively Coupled Plasma Mass Spectroscopy analysis, indicate the reliable operation of the microfiber in vivo. The stretchability of the microfiber, regardless of material composition, is also verified through tensile tests (Figure 3b).

The primary conductive pathway of the microfiber is established by the LM core, resulting in a conductivity comparable to that of the LM itself (3.4×10^4 S cm^{-1}).[30] However, conductivity may vary depending on the nanocomposite composition (Figure 3c). Meanwhile, the stretchability of the microfiber is influenced by the nanocomposite composition. An optimal composition of 25 wt% Ag-Au NWs in the nanocomposite is

**ADVANCED
SCIENCE NEWS**

www.advancedsciencenews.com

**ADVANCED
MATERIALS**

www.advmat.de

identified that maximizes conductivity while preserving the stretchability of the microfiber (Figure 3c, brown). The microfiber exhibits a strain-insensitive property (gauge factor < 1; comparable to bare LM-based devices)[33] due to the fluidic nature of LM, as demonstrated in Figures 3d and S7a–c, Supporting Information. The microfiber maintains structural integrity and conductivity despite repetitive stretching.

One of the key advantages of the nanocomposite is its multi-functionalization potential. Incorporating Pt black microparticles with embossed surface morphologies into the nanocomposite reduces contact impedance at the microfiber–tissue interface, enabling high-quality electrophysiological recording and electrical stimulation (Figure 3e, left). Electrochemical impedance spectroscopy (EIS) measurements confirm reduced impedance due to the Pt black microparticles both in vitro and in vivo (Figure 3f,g). The impedance remains low even under 150% stretching (Figure 3h), ensuring effective charge delivery to dynamically moving organs without performance degradation even during long-term operation. Additionally, low impedance is maintained even after delivering a significant amount of charge (Figure 3i), illustrating its long-term pacing potential. Furthermore, the incorporation of IrO_2 nanoparticles in the nanocomposite provides pH detectability to the microfiber (Figure 3e, right). IrO_2 nanoparticles facilitate reversible redox reactions with hydrogen ions,[50] as evidenced by open circuit potential measurements showing pH dependency under both static and tensile states (Figures 3j,k and S8, Supporting Information). This capability enables pH sensing on dynamically moving organs. In vivo pH sensing tests indicate that the pH values measured in rat's organs are comparable to previously reported values[51–53] (Figure 3l). Real-time monitoring of the rat's stomach successfully detects temporal changes in pH corresponding to food digestion, unaffected by organ motions (Figure 3m).

2.4. Gastric and Muscular Applications of the Microfiber

The advantageous features of the microfiber, such as intrinsic softness, minimally invasive insertion, strain-insensitivity, multi-functionalization, and biocompatibility, are demonstrated by in vivo applications to the stomach and muscles (**Figure 4a**). First, we evaluated the biocompatibility of the microfiber in vitro. The cytotoxic behavior of the microfiber was investigated in vitro using a tetrazolium-based colorimetric assay (MTS assay) with AC16 human cardiomyocyte cells (Figure S9a, Supporting Information). The microfiber showed no significant cytotoxicity compared with the control group (soaked with phosphate-buffered saline solution), regardless of the presence of the liquid metal. To evaluate the biocompatibility of the microfiber in vivo, it was implanted in the intrathoracic region of the rats via intercostal implantation, showing no visible inflammation or displacement over 2 weeks (Figure S9b, Supporting Information). Histologic analyses using anti-CD68 and Masson's trichrome staining also reveal no notable differences in inflammatory cell recruitment or fibrosis, compared to previous reports[45,47] (Figure S9c,d, Supporting Information).

To monitor gastric activity, two microfibers are implanted into the rat's stomach through the abdominal muscle, making contact with the anterior pyloric and corpus regions of the stom-ach, respectively[54] (Figure S10a,b, Supporting Information). Another microfiber served as a reference electrode, positioned near the esophagus region. The microfiber measured electrogastro-grams showed slow waves ranging from 3 to 6 cycles per minute (Figure 4b, left), even under dynamic physiological environments involving breathing and heartbeats[55] (Figure 4b, right). Consequently, differences in cycle lengths and signal amplitudes of electrogastrograms in each diet state (e.g., fasting for 12 h, after finishing a meal, and 2 h after a meal) are successfully moni-tored (Figures 4c,d and S10c, Supporting Information). Besides, the microfiber detects spatial differences in electrogastrogram morphologies across the stomach (Figure S10d, Supporting Information), showing relatively longer cycle length and larger am-plitude in the pyloric region (Figure S10e,f, Supporting Information). Gastric activity can be also effectively modulated using elec-trical stimulation by the microfiber[56] (Figure 4e). A pair of mi-crofibers implanted on the gastric wall proximal to the pylorus successfully accelerated gastric emptying by electrical stimula-tion (Figure 4f). The microfiber can monitor gastric activities and deliver electrical stimulation, simultaneously, even during stom-ach motions (Figure S11, Supporting Information), verifying its diagnostic and therapeutic potential for digestive disorders.

For muscular applications, two pairs of microfibers are im-planted into the biceps femoris and gastrocnemius muscles, which are involved in thigh and calf movements, respectively[57] (Figures 4a,g and S12a, Supporting Information). Each pair of microfibers effectively records the rat's muscular activities, cap-turing rapid leg contraction responses triggered by toe pinching (Figure 4h, red triangle) and foot poking (Figure 4i, red triangle), as well as spontaneous leg relaxation (Figure 4h,i, blue arrow). The spontaneous muscular movement of the rat recovering from anesthesia is also monitored, showing an evolving electromyo-gram (Figure S12b, Supporting Information). As the rat begins to wake up, weak muscle movement is recorded from the lower leg, and once the rat is fully awake and engaged in locomotive movements, continuous and robust signals are recorded from both the thigh and calf muscles.[58] Furthermore, different leg movements can be induced by controlling the amplitude and du-ration of the stimulation[59,60] (Figure S13a,b, Supporting Infor-mation). Electroactive contraction of muscle is allowed through delicate stimulation control (Figure S13c, Supporting Informa-tion), implying the potential of neuromuscular interfaces and bioelectronic prosthetics.[61,62]

2.5. Cardiac Monitoring and Cardiovascular Intervention for Anti-Arrhythmic Treatment

The multifunctional and unique features of the microfiber also enable it to address challenging issues involving the intrathoracic epicardial surface – continuous heart beating, cyclic lung expan-sion, and the presence of various tissues (e.g., skin, rib cages, thoracic muscles, and pericardium) – which impede easy access to the heart with conventional rigid devices.[63,64]

Three types of microfibers are inserted into the myocardium (**Figure 5a,b**) to compare the quality of the recorded electrophysi-ological signals depending on the materials: LM-nanocomposite microfiber with Pt black particles, LM-nanocomposite microfiber without Pt black particles, and LM-only microfiber (Figure 5c,d).
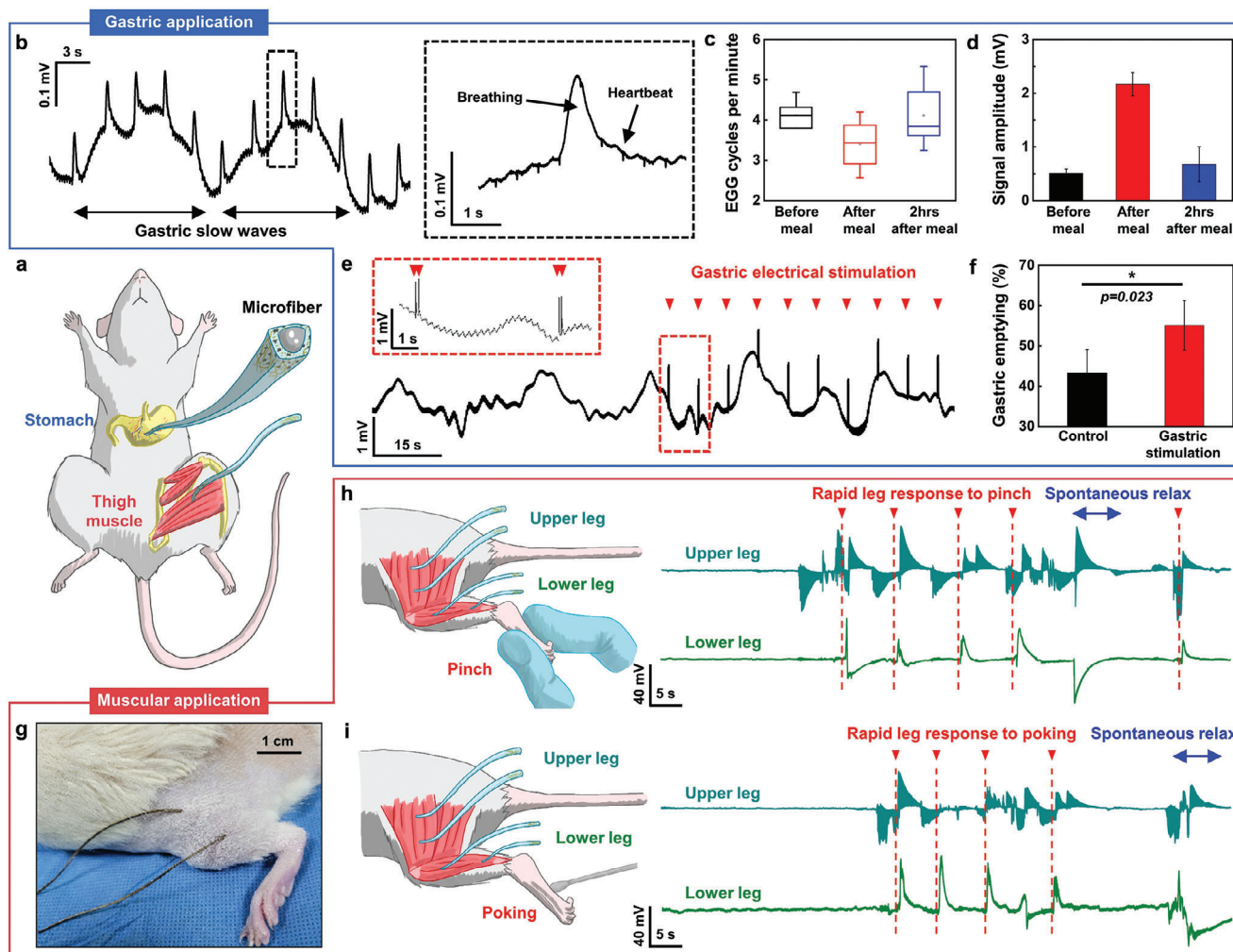
Figure 4. Gastric and muscular application of the microfiber. a) Schematic illustration showing microfibers implanted on the stomach and thigh muscle of the rat. b) Representative example of the recorded electrogastrogram of the rat. The noise from the heartbeat and breathing (inset) was filtered in other figures. c) Gastric slow wave cycles of the rat with different diet status ($n = 8$). d) Amplitude of the electrogastrogram waves of the rats with different diet status ($n = 7$). e) Electrogastrogram recorded from the rat stomach. Gastric electrical stimulation is delivered to the rat's stomach (red triangle). The Inset image shows the magnified timeline of electrogastrogram during electrical stimulation. f) Gastric emptying of the rat with (red bar) and without (black bar) electrical stimulation for 90 min ($n = 6$; *$p \leq 0.05$ for variable of significance). g) Optical image of the rat leg with the implanted microfibers. Electromyogram recorded during the leg contraction of the rat, in response to h) toe pinch and i) foot poking stimulation.

The microfiber containing Pt black microparticles exhibits high-quality electrode-tissue interfacing, enabling noise-free recording as shown in the clear epicardial electrogram morphologies (Figure 5c, red). The LM-nanocomposite microfiber without Pt black microparticles still provides acceptable signals with minimal noise (Figure 5c, black). Notably, the LM-only microfiber yields the worst quality electrograms with a high noise level (Figure 5c, blue).

A similar trend is observed for the strength–duration curves that differentiate between captured pacing (Figure 5e, red) and non-captured stimulation[65] (Figure 5e, blue). The LM-nanocomposite microfiber with Pt black microparticles exhibits the lowest strength–duration curve, which implies that stimulation with lower energy is required for myocardial activation[66] (Figure 5f). Furthermore, the microfiber maintains stable performance for at least 3 weeks, demonstrating long-term operational

reliability (Figures 5g and S14, Supporting Information). These results indicate that the low impedance and efficient charge transfer capability of the functionalized microfiber are advantageous for recording clear cardiac electrograms and stimulating the myocardium effectively, making it a more efficient, long-term, and safer option for cardiac interventions.

The microfiber verifies its capability to acquire high-quality electrograms, distinguishing various arrhythmic rhythms, such as atrial flutter, premature ventricular contraction, monomorphic ventricular tachycardia, and polymorphic ventricular tachycardia (Figure S15, Supporting Information). Moreover, it can detect microcurrents originating from the heart, enabling the diagnosis of electrophysiological disorders, which are challenging to detect accurately amidst surface ECG noise[67,68] (Figure S16a,b, Supporting Information). For example, it facilitates the differential diagnosis of various degrees of atrioventricular (AV) block by
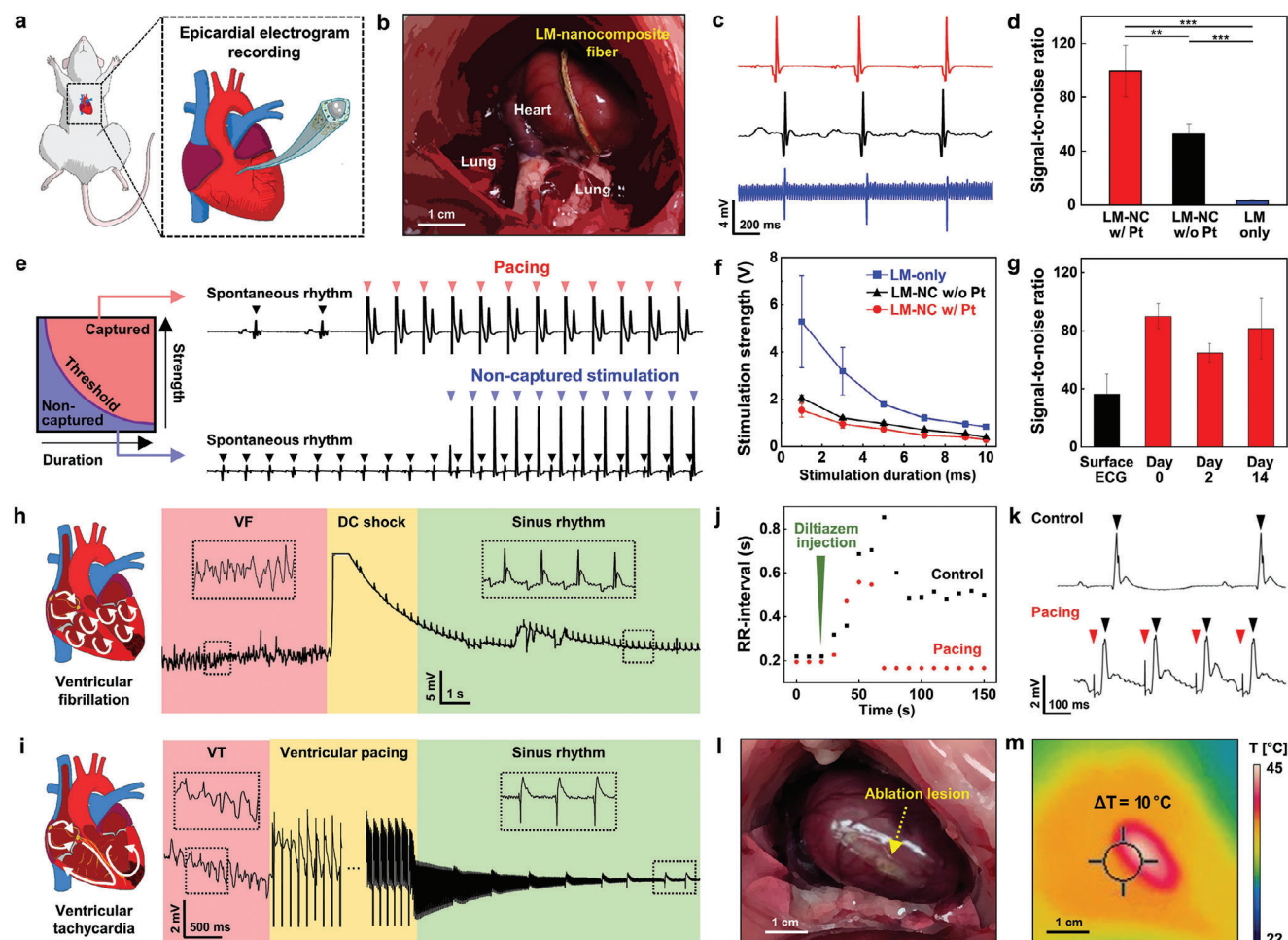
ADVANCED
SCIENCE NEWS

www.advancedsciencenews.com

ADVANCED
MATERIALS

www.advmat.de

Figure 5. Cardiovascular application of the microfiber for diagnosis and treatment of arrhythmias. a) Schematic illustration showing the implanted microfiber for cardiovascular application. b) Optical image showing the thoracic cavity of the rat with the implanted microfiber. c) Epicardial electrogram recorded with various types of microfibers: LM-nanocomposite microfiber with Pt black particles (red), LM-nanocomposite microfiber without Pt black particles (black), and LM-only microfiber (blue). d) Signal-to-noise ratio of epicardial electrogram recorded with various types of microfibers ($n = 9$; **$p \leq 0.01$, ***$p \leq 0.001$ for variables of significance). e) Surface electrocardiogram of the rat during captured pacing (top, red triangles) and non-captured stimulation (bottom, blue triangles). f) Strength–duration curves of the various microfibers measured to determine threshold voltages. g) Temporal changes of the signal-to-noise ratio of the epicardial electrogram ($n = 10$). h) Schematic illustration of ventricular fibrillation (left) and surface ECG of the rat heart during electric shock (right). Consequent restoration of the sinus rhythm was observed. i) Schematic illustration of ventricular tachycardia (left) and surface ECG of the rat heart during 10 Hz ventricular pacing (right). Consequent restoration of the sinus rhythm was observed. j) RR interval of the rat with bradycardia model. Bradycardia was induced after diltiazem injection (green triangle). k) Comparison of surface ECG in the control group (top) and the pacing group (bottom) after bradycardia induction. Ventricular contraction peaks are marked with black triangles, whereas pacing stimulations are marked as red triangles. l) Optical image and m) infrared camera image of the epicardial surface of the rat with increased temperature after radiofrequency ablation.

identifying P waves independent of QRS complexes, indicating a blocked connection between the sinus node and atrioventricular node (Figure S16c–f, Supporting Information).

Cardiac pacing with precisely controlled electrical stimulation from the microfiber is employed to terminate various types of arrhythmic events. Both fatal ventricular fibrillation and sustained ventricular tachycardia are successfully terminated by overdrive pacing (pacing frequency = 10 Hz; amplitude = 1.5 V; pulse width = 10 ms) and a defibrillation shock (amplitude = 20 V, shock duration = 10 ms),[69] respectively (Figures 5h,i and S17a, Supporting Information). The microfiber can manage not only tachyarrhythmias but also bradyarrhythmias by pacing the heart

(Figures 5j and S17b–e, Supporting Information). When diltiazem is administered to two groups of rats (Figure 5j, green triangle), both exhibit an increase in the RR interval. However, the RR interval normalizes solely in the group receiving pacing via the microfiber, aligning with the programmed pacing interval (Figure 5k, bottom), whereas the other group remains at a life-threateningly slow heart rate (Figure 5k, top).

The microfiber can be also employed for radiofrequency ablation, a technique commonly used to eliminate recurrent arrhythmic foci. The intensity of the radiofrequency ablation can be controlled by the input current density of the microfiber, as validated by infrared imaging observations on porcine skin ex vivo

ADVANCED
SCIENCE NEWS

www.advancedsciencenews.com

**ADVANCED
MATERIALS**

www.advmat.de

(Figure S18a, Supporting Information). The local temperature on the rat's myocardial surface in vivo increases significantly (reaching a maximum of 45 °C) with an input power of 20 W (Figure 5l). This temperature is adequate to ablate the arrhythmic substrate (Figures 5m and S18b, Supporting Information), presenting a promising approach for treating cardiac arrhythmias.

3. Conclusions

In this study, we developed a minimally invasive and injectable multifunctional soft bioelectronics, featuring a stretchable conductive microfiber with a LM core and a nanocomposite shell. This microfiber leverages the phase-convertible behavior of LM, allowing it to be easily solidified by freeze-spraying. The high stiffness of the solidified microfiber enables minimally invasive penetration of soft tissues, functioning similar to a conventional needle. Once implanted, the microfiber naturally liquefies, owing to the body temperature in vivo, regaining its original softness and flexibility, ensuring a seamless fit with the curvilinear soft tissues without inducing mechanical mismatch.

Furthermore, the core–shell structure offers the synergistic benefits of both LM and nanocomposite to the microfiber, resulting in high stretchability, exceptional conductivity, strain-insensitivity, and the ability for multi-functionalization. The multifunctionality of the microfiber, including high-quality biosensing and stimulation capabilities, is achieved by integrating auxiliary functional nanoparticles onto the nanocomposite shell. The potential clinical effectiveness of the material design, along with its injectability, is successfully verified through various electroceutical demonstrations on electroactive and dynamic organs, including pH and electrophysiology monitoring and electric stimulation of gastric, peripheral, and cardiac muscles. The practical applications for detection and electroceutical treatment of cardiac arrhythmias validate its high potential and efficacy in clinical medicine.

Despite the groundbreaking characteristics of the microfiber in the field of soft implantable bioelectronics and electronic medicine, several challenges must be addressed before its clinical translation. The facile implementation of the implantation protocol and precise control of the phase transition of the microfiber is imperative for its application to large animal models. While the temporal rigidity of the microfiber can be adjusted depending on the freezing temperature for accurate administration, there is a risk of inducing local frostbite at extremely low temperatures. Future studies should conduct a detailed analysis of the potential hypothermia caused by microfiber implantation. Additionally, comprehensive validation of the functionality, performance, and biocompatibility of the microfiber in large animal models is essential to establishing its clinical applicability.

In addition, further technical developments should also progress toward clinical use. The incorporation of other filler materials into the nanocomposite shell should be demonstrated to showcase the expandable functionality of the microfiber. For example, the therapeutic application of the microfiber can extend to chemotherapy by incorporating functional drug nanoparticles (e.g., targeted drug delivery, and stimulus-responsive drug delivery). However, the efficacy of chemotherapy alone using the microfiber should be taken into consideration due to its low volumetric capacity for drugs. Another option would be to utilize a more advanced microfiber to efficiently treat diseases by combining electrotherapy and chemotherapy or to control the drug release behavior by electric pulse. Further exploration of the interaction between the liquid metal and the nanocomposite shell is also necessary. The in-depth understanding of the mechanistic and electrochemical interaction between the two components of the microfiber,[70,71] such as alloy formation and affinity-interface relationship, could aid in re-optimizing the microfiber design for better performance. Achieving several steps of technology readiness with this new type of bioelectronics will be a key solution for various clinical challenges.

4. Experimental Section

Materials: Gold-coated silver nanowires were synthesized as previously reported.[72] Liquid metal (eutectic gallium-indium), platinum black, and hexylamine were purchased from Sigma Aldrich. Iridium oxide was purchased from Alfa Aesar. Elastomer such as poly(styrene-butylene-styrene) (SBS, KTR 103) was obtained from Kumho Chemicals. Solvents such as ethylene glycol, toluene, hexane, and ethanol were obtained from Samchun Chemicals.

Fabrication of LM-Nanocomposite Microfiber: First, the solution of nanocomposite was prepared by mixing 300 μL of Ag-Au NW in a mixture of ethanol and toluene (1:3 volume ratio) with a concentration of 60 mg mL^{-1}, 2 mg of Pt black, 500 μL of SBS polymer solution (10 wt% in toluene), and 20 μL of hexylamine as a dispersant, in accordance with the optimal nanocomposite composition (25 to 75 of NW wt% to SBS wt%). The solution was then dropped on a silicone (PDMS) mold, filled into the groove of the mold by blade coating, and dried under ambient conditions. The dropping, blade coating, and solvent drying process was repeated four times, forming a nanocomposite film conformally coated on the floor and sidewall. Then, liquid metal was injected into the groove surrounded by the nanocomposite film using a syringe. Next, the nanocomposite solution was dropped, blade coated, and dried five times, forming the top nanocomposite layer smoothly connected with the nanocomposite sidewall. Finally, the fabricated microfiber was detached from the mold. For characterization, the microscopy images and EDS elemental mapping images were taken by SEM (S-3400N, Hitachi) and FE-SEM (JSM-7600F, Jeol), respectively. Cryogenic scanning electron microscopy images were taken by Quanta 3D FEG.

Minimally Invasive Implantation Protocol of the Microfiber: One end of the LM-nanocomposite microfiber was fixed by using a tweezer, and another end of the microfiber was frozen by using Ice spray (Nabakem, Republic of Korea). Freeze-spraying was repetitively applied to the microfiber several times until the microfiber was fully frozen ($T < 0$ °C), when the microfiber was not bent under gravity. Then, the frozen microfiber was directly implanted into the target site without any time delay to prevent thermal equilibrium. After implantation, the frozen microfiber dissolves and restores its original softness and flexibility. Hence, it can be seamlessly integrated into the curved dynamic tissue surface. The arrowhead-shaped anchor was gathered in a frozen state for implantation and unraveled to fix the microfiber at the internal cavity.

Numerical Simulation - Tissue Penetration: Tissue was modeled as a cubic box with 50 mm side length, of which a *xy*-surface was fixed on the wall, meaning that it cannot be deformed. All other surfaces except for the fixed surface can be deformed under loading. The microfiber was modeled as a box with side lengths 700 μm in *x*-, 500 μm in *y*- and 100 mm in *z*–direction. A *xy*-surface of the microfiber and of the tissue contact each other, whose centers were at the same point. Young's modulus of 125 kPa for the tissue, 13 MPa for the microfiber in the liquefied state, and 145 MPa for the device in the frozen state were imposed, determined by the experimental results. Along with Young's modulus, Poisson's ratios of 1 for the tissue and 0.43 for the microfiber in both solidified and liquefied states, respectively, were imposed. A force was loaded on a free *xy*-surface of the microfiber in the *z*–direction until the surface moved by 5 mm in the *z*–direction.

Numerical Simulation - Thermal Equilibrium: The microfiber penetrates the cubic box of the tissue along the z–axis and the penetration length was set to 30 and 5 mm in separate simulations. The thermal conductivity was set to 26.6 W m^{-1} K^{-1} for liquid metal and 94.5 W m^{-1} K^{-1} for nanocomposite; heat capacity was set to 404 J kg^{-1} K^{-1} for liquid metal and 1077 J kg^{-1} K^{-1} for nanowire; and density was set to 6280 kg m^{-3} for liquid metal and 4760 kg m^{-3} for nanowire. The temperature of the heart was fixed at 37 °C during implantation, and the temperature of the solidified microfiber was initially set at −15 °C and subsequently evolved with time. It was assumed that heat transfer occurs only via the conduction. The system's dimensions were aligned with those from the tissue penetration simulation.

Mechanical Characterization: Tensile test was performed to measure the stretchability of the microfiber using the UTM, at a speed of 10 mm min^{-1}, in accordance with a modified version of ISO 527. Both ends of various types of microfibers were adhered on a PET substrate, leaving dimension of width/thickness of 0.8 mm, and length of 5 mm to be stretched. Stretchability of the microfiber was evaluated by identifying the point at which the applied force reached its maximum. This evaluation was performed at a speed of 10 mm min^{-1} under 40% of strain, in accordance with a modified version of ISO 527. The change in elastic modulus of the microfiber was measured by comparing the sampled microfiber before freezing and 30 minutes after dissolving the frozen microfiber.

Electrical Characterization: The conductivity of the microfiber was calculated as follows:

$$\sigma = \frac{1}{R}\frac{L}{A} \tag{1}$$

where σ is conductivity, R is resistance, L is length, and A is cross-sectional area. The resistance was measured using a four-point probe with a Keithley 2450 Sourcemeter, and the cross-sectional area was measured by SEM (S-3400N, Hitachi). The initial length of the microfiber for measuring the conductivity was 1 cm. For the stretching test, each end of the microfiber was connected to a copper wire using silver paste. Then, the microfiber was transferred onto a VHB film (VHB Tape 4910 Clear, 3M) mounted on the uniaxial tensile stage (Jaeil Optical System, Korea). Copper wires were connected to the source meter, and the initial resistance and the resistance at each strain were acquired for calculating the resistance changes. For the cyclic test, repetitive external strain of 40% was applied at a frequency of 0.1 Hz, and the resistance was continuously measured during stretching cycles.

Electrochemical Characterization: EIS measurements were performed by using electrochemical workstation (CHI-660E, CH instruments). Three-electrode system consisting of Ag/AgCl reference electrode, platinum mesh counter electrode, and the microfiber as a working electrode was applied. For comparison, three types of microfibers (LM-SBS microfiber with exposed liquid metal on one side and LM-nanocomposite microfibers with and without Pt black microparticles) were prepared. A.C. impedance measurements were conducted for the frequency range of 10–10 000 Hz, with a potential amplitude of 5 mV, in PBS solution (Dulbecco's phosphate-buffered saline, Sigma Aldrich) and rat interstitial fluid, for in vitro and in vivo tests, respectively. To measure impedance changes under applied strains, the microfiber was stretched and attached to the VHB film. To evaluate the electrochemical performance in long-term use, potential pulse was applied to the microfiber with a pulse width of 1 s, pulse period of 2 s, and pulse amplitude of 1.2 V, in accordance with cardiac pacing conditions in rats.

pH Sensing: The microfiber with pH sensing capability was prepared by replacing the Pt black microparticles with 5 mg of Iridium oxide nanoparticles. Open circuit potential was measured using two-electrode system consisting of the microfiber and platinum mesh electrode. Calibration of the microfiber was conducted in buffer solution with different pH values (Samchun Chemicals). Open circuit potential under tensile strain was measured while the microfiber was stretched and attached to the VHB film. Open circuit potential was measured in rat interstitial fluid and various organs in vivo, including stomach, bladder, and intestine (feces).

Open circuit potential in the 12-h-starved rat's stomach was monitored after food intake.

Radiofrequency Ablation: One end of the microfiber was connected to the electrode tip of radiofrequency generator (MINI-COAG, ITC Co.). For the monopolar radiofrequency ablation in rat's heart, the microfiber was implanted on the epicardia surface and high frequency current (55 kHz, 20 W) was induced for 10 s.

In Vitro Cytotoxicity Assay: The viability of cells exposed to the microfiber was evaluated using the MTS ((3-(4,5-dimethylthiazol-2-yl)−5-(3-carboxymethoxyphenyl)−2-(4-sulfophenyl)−2H-tetrazolium, Promega, USA) assay. The microfibers with and without liquid metal were attached to the side wall of each 96-well plate to prevent physical damage to the cells. Cell medium was then prepared in each well, and AC16 human cardiomyocyte cells were cultured in each well. The cells were placed in an incubator with 5% CO_2 at 37 °C, and the MTS assay was used to test the viability after 1 day of culture. The medium was replaced with 100 μL of fresh medium containing the MTS solution. After 1 h of incubation at 37 °C, the MTS medium was removed and replaced with 100 μL of dimethyl sulfoxide (Sigma Aldrich, USA). Optical density (OD) was measured at 490 nm using a multi-plate reader (SpectraMax M3, Molecular Devices, USA).

Biocompatibility Analysis: For the histological analysis, the 1 cm-length LM-nanocomposite microfiber and nanocomposite microfiber were subcutaneously implanted in the lower back region of the 8-week-old Sprague-Dawley (SD) rats (Orient Bio Inc., Korea). After 2 weeks from implantation, rats were euthanized, and the full extraction of skin tissue was performed. The extracted tissue was fixed in the 35% formalin solution. Such tissues were dehydrated with ethanol and then infiltrated and embedded in paraffin. Afterward, paraffin blocks were serially sectioned by a microtome (Leica, Germany) into 4 μm-thick coronal sections and then collected on slide glasses. Then, they were processed under Anti-CD68 staining and Masson's trichrome staining to evaluate the inflammatory response induced by the implantation of the microfiber. The stained tissue slides were imaged by optical microscope.

Muscular Experiment Protocol: The 8-week-old male SD rats (Orient Bio Inc., Korea) were anesthetized with 3–5% isoflurane chamber. The anesthesia level was kept with the gas mask after clipping hairs of the thigh region. Sterilization of the hair removal region using 70% ethanol and iodine solution was followed. 18G catheter pathway was made at the proximal thigh region in 1 cm-depth using 18G syringe needle to make pathway for the microfiber implantation. After the removal of the needle, the microfiber was implanted in the thigh muscles through the catheter. The protocol was repeated 2 cm distal from the initial implantation. The end of the microfiber was connected to the commercialized data acquisition (DAQ) device, Power Lab (AD Instruments, New Zealand). While recording muscular motion, mild toe pinch and toe poking were performed.

Gastric Experiment Protocol: The 8 week-old male SD rats (Orient Bio Inc., Korea) were anesthetized with 3–5% isoflurane chamber. The anesthesia level was kept with the gas mask after clippering hairs of the upper abdominal region. The skin 10 cm below the xiphoid process was poked with 18G needle to make microfiber insertion point. The frozen microfiber was then implanted to the skin hole for the implantation. The tissue incision or endoscopy was used to confirm the location of the microfiber in the cavity. The end of the microfiber was connected to the commercialized DAQ device, Power Lab (AD Instruments, New Zealand).

Cardiac Experiment Protocol: The 8 week-old male SD rats (Orient Bio Inc., Korea) were anesthetized with 3–5% isoflurane chamber. Hair removal using clipper was followed by administration of the commercialized hair removal cream on the left thoracic region.[73] The skin of the intercostal region between third and fourth rib was poked with 18G needle. Then the frozen microfiber was implanted through the skin hole while monitored by commercialized echocardiography (Accuvix V10, Medison) or the portable endoscope. After two microfibers were implanted on the desired location of the epicardial surface, other ends of the microfibers were connected to the commercialized DAQ device, Power Lab (AD Instruments, New Zealand). Norepinephrine was injected intravenously to induce tachyarrhythmias. Otherwise, the diltiazem solution was injected intravenously to induce bradyarrhythmia. To deliver electric stimulation, the pair of microfibers was connected to the current output channel of the

2404101 (10 of 12)

© 2024 The Author(s). Advanced Materials published by Wiley-VCH GmbH

DAQ device, Power Lab (AD Instruments, New Zealand). The surface ECG was recorded during stimulation.

Statistical Analysis: All data were analyzed by two-sample *t*-test. All statistical indications in the graph were presented as mean with standard deviation. Sample size (*n*) = 3 for experimental data, unless otherwise noted in the figure caption. Statistical analysis results such as *p*-value are described in each figure caption. A *p*-value < 0.05 was considered statistically significant.

Ethical Approval: This study was approved by the Institutional Animal Care and Use Committee (SNU-221102-3) and was performed in accordance with the IACUC guidelines and with the National Institute of Health Guide for the Care and Use of Laboratory Animals.

Supporting Information

Supporting Information is available from the Wiley Online Library or from the author.

Acknowledgements

Conflict of Interest

The authors declare no conflict of interest.

Data Availability Statement

The data that support the findings of this study are available from the corresponding author upon reasonable request.

Keywords

[1] K. W. Cho, S.-H. Sunwoo, Y. J. Hong, J. H. Koo, J. H. Kim, S. Baik, T. Hyeon, D.-H. Kim, *Chem. Rev.* **2022**, *122*, 5068.

[2] S.-H. Sunwoo, S. I. Han, C. S. Park, J. H. Kim, J. S. Georgiou, S.-P. Lee, D.-H. Kim, T. Hyeon, *Nat. Rev. Bioeng.* **2024**, *2*, 8.

[3] Y. Jiang, S. Ji, J. Sun, J. Huang, Y. Li, G. Zou, T. Salim, C. Wang, W. Li, H. Jin, J. Xu, S. Wang, T. Lei, X. Yan, W. Y. X. Peh, S.-C. Yen, Z. Liu, M. Yu, H. Zhao, Z. Lu, G. Li, H. Gao, Z. Liu, Z. Bao, X. Chen, *Nature* **2023**, *614*, 456.

[4] J. Koo, M. R. MacEwan, S.-K. Kang, S. M. Won, M. Stephen, P. Gamble, Z. Xie, Y. Yan, Y.-Y. Chen, J. Shin, N. Birenbaum, S. Chung, S. B. Kim, J. Khalifeh, D. V. Harburg, K. Bean, M. Paskett, J. Kim, Z. S. Zohny, S. M. Lee, R. Zhang, K. Luo, B. Ji, A. Banks, H. M. Lee, Y. Huang, W. Z. Ray, J. A. Rogers, *Nat. Med.* **2018**, *24*, 1830.

[5] Y. H. Jung, J. U. Kim, J. S. Lee, J. H. Shin, W. Jung, J. Ok, T. Kim, *Adv. Mater.* **2020**, *32*, 1907478.

[6] A. Sahasrabudhe, L. E. Rupprecht, S. Orguc, T. Khudiyev, T. Tanaka, J. Sands, W. Zhu, A. Tabet, M. Manthey, H. Allen, G. Loke, M.-J. Antonini, D. Rosenfeld, J. Park, I. C. Garwood, W. Yan, F. Niroui, Y. Fink, A. Chandrakasan, D. V. Bohórquez, P. Anikeeva, *Nat. Biotechnol.* **2023**, https://doi.org/10.1038/s41587-023-01833-5.

[7] S. Choi, S. I. Han, D. Kim, T. Hyeon, D.-H. Kim, *Chem. Soc. Rev.* **2019**, *48*, 1566.

[8] H. Choi, Y. Kim, S. Kim, H. Jung, S. Lee, K. Kim, H.-S. Han, J. Y. Kim, M. Shin, D. Son, *Nat. Electron.* **2023**, *6*, 779.

[9] J. H. Koo, J. Song, S. Yoo, S. Sunwoo, D. Son, D. Kim, *Adv. Mater. Technol.* **2020**, *5*, 2000407.

[10] D. Jung, C. Lim, H. J. Shim, Y. Kim, C. Park, J. Jung, S. I. Han, S.-H. Sunwoo, K. W. Cho, G. D. Cha, D. C. Kim, J. H. Koo, J. H. Kim, T. Hyeon, D.-H. Kim, *Science* **2021**, *373*, 1022.

[11] S. Song, K. Y. Kim, S. H. Lee, K. K. Kim, K. Lee, W. Lee, H. Jeon, S. H. Ko, *Adv. NanoBiomed Res.* **2022**, *2*, 2100111.

[12] Y. Ohm, C. Pan, M. J. Ford, X. Huang, J. Liao, C. Majidi, *Nat. Electron.* **2021**, *4*, 185.

[13] Z. Jiang, N. Chen, Z. Yi, J. Zhong, F. Zhang, S. Ji, R. Liao, Y. Wang, H. Li, Z. Liu, Y. Wang, T. Yokota, X. Liu, K. Fukuda, X. Chen, T. Someya, *Nat. Electron.* **2022**, *5*, 784.

[14] S. Park, H. Yuk, R. Zhao, Y. S. Yim, E. W. Woldeghebriel, J. Kang, A. Canales, Y. Fink, G. B. Choi, X. Zhao, P. Anikeeva, *Nat. Commun.* **2021**, *12*, 3435.

[15] S. Wang, J. Xu, W. Wang, G.-J. N. Wang, R. Rastak, F. Molina-Lopez, J. W. Chung, S. Niu, V. R. Feig, J. Lopez, T. Lei, S.-K. Kwon, Y. Kim, A. M. Foudeh, A. Ehrlich, A. Gasperini, Y. Yun, B. Murmann, J. B. H. Tok, Z. Bao, *Nature* **2018**, *555*, 83.

[16] G. Li, K. Huang, J. Deng, M. Guo, M. Cai, Y. Zhang, C. F. Guo, *Adv. Mater.* **2022**, *34*, 2200261.

[17] C. M. Tringides, N. Vachicouras, I. de Lázaro, H. Wang, A. Trouillet, B. R. Seo, A. Elosegui-Artola, F. Fallegger, Y. Shin, C. Casiraghi, K. Kostarelos, S. P. Lacour, D. J. Mooney, *Nat. Nanotechnol.* **2021**, *16*, 1019.

[18] D. Jung, Y. Kim, H. Lee, S. Jung, C. Park, T. Hyeon, D. Kim, *Adv. Mater.* **2023**, *35*, 2303458.

[19] H. J. Kim, D. Jung, S.-H. Sunwoo, S. Jung, J. H. Koo, D.-H. Kim, *Adv. NanoBiomed Res.* **2023**, *3*, 2200153.

[20] N. Matsuhisa, D. Inoue, P. Zalar, H. Jin, Y. Matsuba, A. Itoh, T. Yokota, D. Hashizume, T. Someya, *Nat. Mater.* **2017**, *16*, 834.

[21] S. Wang, Y. Nie, H. Zhu, Y. Xu, S. Cao, J. Zhang, Y. Li, J. Wang, X. Ning, D. Kong, *Sci. Adv.* **2022**, *8*, eabl5511.

[22] K.-C. Agno, K. Yang, S.-H. Byun, S. Oh, S. Lee, H. Kim, K. Kim, S. Cho, W.-I. Jeong, J.-W. Jeong, *Nat. Biomed. Eng.* **2023**, https://doi.org/10.1038/s41551-023-01116-z.

[23] F. Krisnadi, L. L. Nguyen, J. M. Ankit, M. R. Kulkarni, N. Mathews, M. D. Dickey, *Adv. Mater.* **2020**, *32*, 2001642.

[24] A. Leber, C. Dong, R. Chandran, T. Das Gupta, N. Bartolomei, F. Sorin, *Nat. Electron.* **2020**, *3*, 316.

[25] S. Gong, L. W. Yap, B. Zhu, Q. Zhai, Y. Liu, Q. Lyu, K. Wang, M. Yang, Y. Ling, D. T. H. Lai, F. Marzbanrad, W. Cheng, *Adv. Mater.* **2019**, *31*, 1903789.

[26] D. Jung, C. Lim, C. Park, Y. Kim, M. Kim, S. Lee, H. Lee, J. H. Kim, T. Hyeon, D. Kim, *Adv. Mater.* **2022**, *34*, 2200980.

[27] H. Kim, A. Thukral, S. Sharma, C. Yu, *Adv. Mater. Technol.* **2018**, *3*, 11800043.

[28] W. Lee, H. Kim, I. Kang, H. Park, J. Jung, H. Lee, H. Park, J. S. Park, J. M. Yuk, S. Ryu, J.-W. Jeong, J. Kang, *Science* **2022**, *378*, 637.

[29] Q. Shen, M. Jiang, R. Wang, K. Song, M. H. Vong, W. Jung, F. Krisnadi, R. Kan, F. Zheng, B. Fu, P. Tao, C. Song, G. Weng, B. Peng, J. Wang, W. Shang, M. D. Dickey, T. Deng, *Science* **2023**, *379*, 488.

[30] T. Daeneke, K. Khoshmanesh, N. Mahmood, I. A. de Castro, D. Esrafilzadeh, S. J. Barrow, M. D. Dickey, K. Kalantar-zadeh, *Chem. Soc. Rev.* **2018**, *47*, 4073.

**ADVANCED
SCIENCE NEWS**

www.advancedsciencenews.com

**ADVANCED
MATERIALS**

www.advmat.de

[31] G. Li, M. Zhang, S. Liu, M. Yuan, J. Wu, M. Yu, L. Teng, Z. Xu, J. Guo, G. Li, Z. Liu, X. Ma, *Nat. Electron.* **2023**, *6*, 154.

[32] E. J. Markvicka, M. D. Bartlett, X. Huang, C. Majidi, *Nat. Mater.* **2018**, *17*, 618.

[33] C. Hang, L. Ding, S. Cheng, R. Dong, J. Qi, X. Liu, Q. Liu, Y. Zhang, X. Jiang, *Adv. Mater.* **2021**, *33*, 2101447.

[34] G.-H. Lee, D. H. Lee, W. Jeon, J. Yoon, K. Ahn, K. S. Nam, M. Kim, J. K. Kim, Y. H. Koo, J. Joo, W. Jung, J. Lee, J. Nam, S. Park, J.-W. Jeong, S. Park, *Nat. Commun.* **2023**, *14*, 4173.

[35] X. Sun, B. Yuan, H. Wang, L. Fan, M. Duan, X. Wang, R. Guo, J. Liu, *Adv. NanoBiomed Res.* **2021**, *1*, 2000086.

[36] L. Mou, J. Qi, L. Tang, R. Dong, Y. Xia, Y. Gao, X. Jiang, *Small* **2020**, *16*, 2005336.

[37] S. Park, Y. Guo, X. Jia, H. K. Choe, B. Grena, J. Kang, J. Park, C. Lu, A. Canales, R. Chen, Y. S. Yim, G. B. Choi, Y. Fink, P. Anikeeva, *Nat. Neurosci.* **2017**, *20*, 612.

[38] S. Jin, H. Choi, D. Seong, C.-L. You, J.-S. Kang, S. Rho, W. B. Lee, D. Son, M. Shin, *Nature* **2023**, *623*, 58.

[39] G. D. Cha, M. Kim, O. K. Park, S. Sunwoo, T. Kang, W. H. Lee, S. Nam, T. Hyeon, S. H. Choi, D. Kim, *Small Methods* **2023**, *7*, 2300032.

[40] D.-H. Kim, N. Lu, R. Ghaffari, Y.-S. Kim, S. P. Lee, L. Xu, J. Wu, R.-H. Kim, J. Song, Z. Liu, J. Viventi, B. de Graff, B. Elolampi, M. Mansour, M. J. Slepian, S. Hwang, J. D. Moss, S.-M. Won, Y. Huang, B. Litt, J. A. Rogers, *Nat. Mater.* **2011**, *10*, 316.

[41] Z. Zhao, S. Soni, T. Lee, C. A. Nijhuis, D. Xiang, *Adv. Mater.* **2023**, *35*, 2203391.

[42] H. Li, R. Qu, Z. Ma, N. Zhou, Q. Huang, Z. Zheng, *Adv. Funct. Mater.* **2023**, 2308120.

[43] C. Lu, S. Park, T. J. Richner, A. Derry, I. Brown, C. Hou, S. Rao, J. Kang, C. T. Moritz, Y. Fink, P. Anikeeva, *Sci. Adv.* **2017**, *3*, 1600955.

[44] S. Choi, J. Park, W. Hyun, J. Kim, J. Kim, Y. B. Lee, C. Song, H. J. Hwang, J. H. Kim, T. Hyeon, D.-H. Kim, *ACS Nano* **2015**, *9*, 6626.

[45] S. Choi, S. I. Han, D. Jung, H. J. Hwang, C. Lim, S. Bae, O. K. Park, C. M. Tschabrunn, M. Lee, S. Y. Bae, J. W. Yu, J. H. Ryu, S.-W. Lee, K. Park, P. M. Kang, W. B. Lee, R. Nezafat, T. Hyeon, D.-H. Kim, *Nat. Nanotechnol.* **2018**, *13*, 1048.

[46] S.-H. Sunwoo, M.-J. Cha, S. I. Han, H. Kang, Y. S. Cho, D.-H. Yeom, C. S. Park, N. K. Park, S. W. Choi, S. J. Kim, G. D. Cha, D. Jung, S. Choi, S. Oh, G.-B. Nam, T. Hyeon, D.-H. Kim, S.-P. Lee, *Sci. Adv.* **2023**, *9*, eadf6856.

[47] S.-H. Sunwoo, S. I. Han, D. Jung, M. Kim, S. Nam, H. Lee, S. Choi, H. Kang, Y. S. Cho, D.-H. Yeom, M.-J. Cha, S. Lee, S.-P. Lee, T. Hyeon, D.-H. Kim, *ACS Nano* **2023**, *17*, 7550.

[48] M. Han, L. Chen, K. Aras, C. Liang, X. Chen, H. Zhao, K. Li, N. R. Faye, B. Sun, J.-H. Kim, W. Bai, Q. Yang, Y. Ma, W. Lu, E. Song, J. M. Baek, Y. Lee, C. Liu, J. B. Model, G. Yang, R. Ghaffari, Y. Huang, I. R. Efimov, J. A. Rogers, *Nat. Biomed. Eng.* **2020**, *4*, 997.

[49] G. D. Cha, W. H. Lee, S.-H. Sunwoo, D. Kang, T. Kang, K. W. Cho, M. Kim, O. K. Park, D. Jung, J. Lee, S. H. Choi, T. Hyeon, D.-H. Kim, *ACS Nano* **2022**, *16*, 554.

[50] M. T. Ghoneim, A. Nguyen, N. Dereje, J. Huang, G. C. Moore, P. J. Murzynowski, C. Dagdeviren, *Chem. Rev.* **2019**, *119*, 5248.

[51] A. C. B. Paula, J. S. Gracioso, W. Toma, R. Bezerra, M. A. J. Saad, I. M. S. De Lucca, E. M. Carneiro, A. R. M. S. Brito, *Br. J. Nutr.* **2005**, *93*, 47.

[52] W. Lu, M. Wu, J. Zhang, T. Huang, S. Du, Y. Cao, *PLoS One* **2021**, *16*, 0257012.

[53] K. Tomochika, S. Shinoda, H. Kumon, M. Mori, Y. Moriyama, M. Futai, *FEBS Lett.* **1997**, *404*, 61.

[54] J. Keller, G. Bassotti, J. Clarke, P. Dinning, M. Fox, M. Grover, P. M. Hellström, M. Ke, P. Layer, C. Malagelada, H. P. Parkman, S. M. Scott, J. Tack, M. Simren, H. Törnblom, M. Camilleri, *Nat. Rev. Gastroenterol. Hepatol.* **2018**, *15*, 291.

[55] N. Wolpert, I. Rebollo, C. Tallon-Baudry, *Psychophysiology* **2020**, *57*, 13599.

[56] L. K. Cheng, N. D. Nagahawatte, R. Avci, P. Du, Z. Liu, N. Paskaranandavadivel, *Front. Neurosci.* **2021**, *15*, 645472.

[57] A. Rainoldi, G. Melchiorri, I. Caruso, *J. Neurosci. Methods* **2004**, *134*, 37.

[58] Y. Huang, H. Li, T. Hu, J. Li, C. K. Yiu, J. Zhou, J. Li, X. Huang, K. Yao, X. Qiu, Y. Zhou, D. Li, B. Zhang, R. Shi, Y. Liu, T. H. Wong, M. Wu, H. Jia, Z. Gao, Z. Zhang, J. He, M. Zheng, E. Song, L. Wang, C. Xu, X. Yu, *Nano Lett.* **2022**, *22*, 5944.

[59] J. Deng, H. Yuk, J. Wu, C. E. Varela, X. Chen, E. T. Roche, C. F. Guo, X. Zhao, *Nat. Mater.* **2021**, *20*, 229.

[60] C. Lim, C. Park, S.-H. Sunwoo, Y. G. Kim, S. Lee, S. I. Han, D. Kim, J. H. Kim, D.-H. Kim, T. Hyeon, *ACS Nano* **2022**, *16*, 10431.

[61] D. Afanasenkau, D. Kalinina, V. Lyakhovetskii, C. Tondera, O. Gorsky, S. Moosavi, N. Pavlova, N. Merkulyeva, A. V. Kalueff, I. R. Minev, P. Musienko, *Nat. Biomed. Eng.* **2020**, *4*, 1010.

[62] T. Zhou, H. Yuk, F. Hu, J. Wu, F. Tian, H. Roh, Z. Shen, G. Gu, J. Xu, B. Lu, X. Zhao, *Nat. Mater.* **2023**, *22*, 895.

[63] A. Burton, Z. Wang, D. Song, S. Tran, J. Hanna, D. Ahmad, J. Bakall, D. Clausen, J. Anderson, R. Peralta, K. Sandepudi, A. Benedetto, E. Yang, D. Basrai, L. E. Miller, M. C. Tresch, P. Gutruf, *Nat. Commun.* **2023**, *14*, 7887.

[64] Y. Li, N. Li, W. Liu, A. Prominski, S. Kang, Y. Dai, Y. Liu, H. Hu, S. Wai, S. Dai, Z. Cheng, Q. Su, P. Cheng, C. Wei, L. Jin, J. A. Hubbell, B. Tian, S. Wang, *Nat. Commun.* **2023**, *14*, 4488.

[65] S. Coates, B. Thwaites, *Pacing Clin. Electrophysiol.* **2000**, *23*, 1273.

[66] S. Oh, W.-Y. Kim, H. C. Kim, I.-Y. Oh, E.-K. Choi, *Heart Rhythm* **2011**, *8*, 1637.

[67] K. Sim, F. Ershad, Y. Zhang, P. Yang, H. Shim, Z. Rao, Y. Lu, A. Thukral, A. Elgalad, Y. Xi, B. Tian, D. A. Taylor, C. Yu, *Nat. Electron.* **2020**, *3*, 775.

[68] M. Sugiyama, T. Uemura, M. Kondo, M. Akiyama, N. Namba, S. Yoshimoto, Y. Noda, T. Araki, T. Sekitani, *Nat. Electron.* **2019**, *2*, 351.

[69] J. Ausra, M. Madrid, R. T. Yin, J. Hanna, S. Arnott, J. A. Brennan, R. Peralta, D. Clausen, J. A. Bakall, I. R. Efimov, P. Gutruf, *Sci. Adv.* **2022**, *8*, eabq7469.

[70] T. T. Nguyen, P. Zhang, J. Bi, N. H. Nguyen, Y. Dang, Z. Xu, H. Wang, N. Ninan, R. Bright, T. Pham, C. K. Nguyen, Y. Sabri, M. T. Nguyen, J. Vongsvivut, Y. Zhao, K. Vasilev, V. K. Truong, *Adv. Funct. Mater.* **2023**, 2310539.

[71] Y. Lai, H. Lu, H. Wu, D. Zhang, J. Yang, J. Ma, M. Shamsi, V. Vallem, M. D. Dickey, *Adv. Energy Mater.* **2021**, *11*, 2100411.

[72] S. Sunwoo, S. I. Han, H. Kang, Y. S. Cho, D. Jung, C. Lim, C. Lim, M. Cha, S. Lee, T. Hyeon, D. Kim, *Adv. Mater. Technol.* **2020**, *5*, 1900768.

[73] R. T. Yin, S. W. Chen, K. Benjamin Lee, Y. S. Choi, J. Koo, Q. Yang, M. A. Napolitano, J. Ausra, T. J. Holleran, J. B. Lapiano, E. Alex Waters, A. Brikha, G. Kowalik, A. N. Miniovich, H. S. Knight, B. A. Russo, A. Kiss, A. Murillo-Berlioz, T. Efimova, C. R. Haney, P. Gutruf, J. A. Rogers, G. D. Trachiotis, I. R. Efimov, *Nat. Protoc.* **2022**, *18*, 374.

2404101 (12 of 12)